Check for updates

Nanocellulose films with multiple functional nanoparticles in confined spatial distribution†

Soledad Roig-Sanchez, [iD] [a] Erik Jungstedt, [b] Irene Anton-Sales, [iD] [a] David C. Malaspina, [iD] [a] Jordi Faraudo, [iD] [a] Lars A. Berglund, [iD] [b] Anna Laromaine [iD] [a] and Anna Roig [iD] *[a]

Industries, governments and consumers increasingly request sustainable resources and greener routes for the integration of advanced functional nanocomposites in products and devices. Among renewable biopolymers, cellulose deserves special consideration since it is the most abundant one. While inorganic nanoparticles add functional properties to a nanocomposite, a flexible and porous cellulosic support will facilitate the interaction of the nanoparticles with the surroundings, their handling and recycling. A significant challenge is to develop high strength, flexible nanobiocomposites controlling the nanoparticle properties, their volume fraction and their topographic distribution within the scaffold. A new concept is presented here for multifunctional laminates where layers consist of bacterial cellulose fibrils decorated by inorganic nanoparticles. Each layer can provide a specific function using a different nanoparticle. As model systems, we have selected two metals (Au, Ag) and two semiconductors (TiO_2 and Fe_2O_3). Energy-efficient microwave-assisted synthetic routes have been used to *in situ* nucleate and grow the inorganic nanocrystals on the cellulose fibrils. Then, functionalized bacterial cellulose films can be arranged as laminates in a millefeuille construct simply by layering and drying the wet films at 60 °C. After drying, they perform as a single integrated and thicker film. Structural, functional and mechanical integrity of the laminates have been investigated. Molecular dynamics simulations were used to compute the surface adhesion energy between two cellulose fibrils and the results are discussed in light of the experimental peel-off data for the separation of the layers in the laminate.

Conceptual insights

Unique properties of bacterial cellulose, specifically the nanometric dimensions of the chemically modifiable hydrophilic fibrils and the 3D interwoven nature of the pellicle network, have inspired a facile concept of creating multifunctional nanocellulose laminates. These constructs are based on layers of bacterial cellulose strongly bonded and with the cellulose fibrils in each layer decorated by specific inorganic nanoparticles, thus providing a topographic order of the particles resembling a flexible millefeuille. The approach enlarges the materials design scope for functional nanocelluloses so that several nanotechnologies could be integrated in one material. The proposed modular laminates can be *ad libitum* assembled by means of molecular scale cellulose–cellulose adhesion during film drying. Forces involved in the self-adhesive behavior of two layers have been experimentally computed using peel off tests and compared with values resulting from molecular dynamics simulation.

1. Introduction

Cellulose is an almost inexhaustible biopolymer of widespread use since prehistoric times. Interestingly, nanocelluloses combine cellulose's properties with the high surface area of nanomaterials. Increasing demand for cost-effective renewable high-performance materials makes nanocelluloses attractive for advanced applications in many sectors ranging from photonics,[1] to food packaging,[2] flexible electronics[3] or health.[4] Cellulose nanocrystals and individual nanofibrils derived from plants are obtained after processing, which may require high energy and chemicals that are not eco-friendly. Another class of nanocellulose is bacterial cellulose (BC) that is readily produced in pure form by microorganisms. In BC, the elementary fibrils have a diameter between 1.5 and 3.5 nm, the microfibrils between 10 and 30 nm and the microfibrillar bands have a width of ~100 nm and many micrometres in length. In the present text, the term "fibril" is used for these fibrous entities. BC also presents higher crystallinity than cellulose fibrils from wood fibres or parenchyma cells (*i.e.*, 65–80% for BC compared to 40–55% for dissolved pulp).[5] Among the many organisms extracellularly producing cellulose, the bacteria *Komagataeibacter xylinus* (*K. xylinus*) is an extremely efficient one.[6,7]

During BC's biosynthesis in static conditions, high aspect ratio bacterial cellulose's fibrils are interwoven to form a stable and non-soluble 3D-porous network that grows as a flat film at the liquid-air interface also known as fleece or pellicle.

[a] *Institut de Ciència de Materials de Barcelona (ICMAB), Campus UAB, Bellaterra, Catalonia, E-08193, Spain. E-mail: roig@icmab.es*

[b] *Department of Fiber and Polymer Technology, Wallenberg Wood Science Center, Royal Institute of Technology (KTH), SE-100 44 Stockholm, Sweden*

† Electronic supplementary information (ESI) available: Experimental section, supplementary figures and videos. See DOI: 10.1039/c8nh00310f

Moreover, nanocomposites,[8] film microstructuration[9] and non-flat 3D geometries[10,11] can also be attained during the biosynthetic process. Bacterial cellulose films are characterized by their light weight, transparency, thermal stability up to ~280 °C, high mechanical flexibility and remarkably high tensile strength together with an exceptional liquid absorption capacity (up to 100 times its own weight in water), biocompatibility and non-immunogenicity.[12] Inorganic nanoparticles can be combined with the chemically modifiable cellulose nanofibrils to constitute new products and devices. Recent reviews have highlighted the preparation and applications of nanocelluloses (including bacterial cellulose) as versatile supports for nanoparticles to be applied in catalysis,[13] sensors,[14] functional food packaging,[15] or medical uses.[16] However, inhomogeneous particle disposition or weak nanoparticle attachment are major reported drawbacks.[17,18]

In this work, we increased the material design scope for multifunctional nanocellulose using a laminate concept that takes advantage of the self-adhesive behaviour of wet BC films upon drying. The laminate is formed by BC layers, which have different functions endowed by the specific inorganic nanoparticles decorating the cellulose fibres. Each layer spatially confines the nanoparticles across the whole cross-section of the film. Thus, the nanoparticle-decorated bacterial cellulose layers could be *ad libitum* arranged as a millefeuille laminate simply by drying the films in the desired order. Next, we assessed the functional and mechanical integrity of the millefeuille laminate. Specifically, we used confocal and electron microscopy to investigate the layer interfaces and a peel off test to evaluate surface adhesion energy between the different functional layers during delamination process. In addition, surface adhesion energy of two crystalline cellulose fibrils has been studied by molecular dynamic simulations and the results are discussed in light of the experimental peel off data.

2. Results and discussion

Functional cellulose nanocomposites are particularly attractive since the resulting nanomaterial can synergistically exploit the characteristics of both components; the electronic, optical, magnetic, catalytic or bioactivity properties provided by the nanoparticles and the outstanding structural characteristics of the bacterial cellulose (fibrous and mesoporous microstructure, flexibility and high fibre tensile strength,...). The laminate created here contain different nanoparticles with complementary properties but also spatial confinement thus enlarging the materials design space for multifunctional nanocelluloses. Two metals (Au, Ag) and two semiconductors (TiO$_2$ and Fe$_2$O$_3$) were selected as model systems. Bacterial cellulose-based nanocomposites with Ag and TiO$_2$ have been reported for antibacterial applications.[19,20] TiO$_2$ and Au nanocomposites were applied in catalysis[21–23] while sensing applications were also reported for BC–Au.[24] BC with Fe$_2$O$_3$ nanoparticles[25,26] was proposed as radio-frequency shielding materials,[27] anti-counterfeiting papers,[28] ultra-thin loudspeakers[29] or for heavy metal removal.[30]

In our approach, metal and metal oxide nanoparticles decorate the bacterial cellulose fibrils. This is accomplished by *in situ* preparation through energy efficient microwave-assisted syntheses. Microwave heating represents an attractive synthetic route for colloidal chemistry in terms of energy and reagents costs, due to the favourable kinetics and high yield resulting from the chemical reactions.[31–33] Compared to other heating methods, microwave radiation avoids temperature gradients within the vessel and promotes synchronic nucleation and growth. Moreover, the hydroxyl groups of the cellulose fibrils may act as selective nucleation sites providing homogeneous nanocrystal distribution in the material volume. We have previously shown that microwave-assisted thermal decomposition is an efficient and fast method to attain uniform and controllable iron oxide nanoparticles content in BC films while preserving the flexibility of the cellulose and avoiding leaching of the inorganic phase during the *in operando* conditions in liquids.[25] In this study, we have extended the approach to other nanoparticle (NP) systems (Au, Ag and TiO$_2$) and developed a lamination strategy for multifunctional nanomaterials.

A detailed description on the bacterial cellulose harvesting, the microwave synthetic routes employed to functionalize the BC layers and their characterization are provided in the Experimental section of the ESI.† Fig. 1A includes images of wet BC films composed with Ag, TiO$_2$, Fe$_2$O$_3$ and Au NPs. Films show a uniform characteristic colour from each nanoparticle. Scanning and transmission electron microscopy (SEM and TEM) micrographs show the cellulose ribbons decorated with the respective nanoparticles, Fig. 1B and C. Images evidence that the inorganic nanoparticles are homogeneously distributed along the fibrils. Differences in nanoparticle content are observed depending on the nanoparticle system and the reaction mechanism for each material (Table S1 contains the proposed reaction mechanism, ESI†). Moreover, by increasing the initial precursor concentration is possible to increase the final nanoparticle content in the films as shown in Table S1 (ESI†). Thermal gravimetric analysis (TGA) (Fig. S1, ESI†) quantifies the nanoparticle content of the nanocomposites (5, 33, 32, 3 wt% or 0.2, 2.7, 4.7, 0.6 vol% for Au, Ag, Fe$_2$O$_3$ and TiO$_2$ respectively). Fig. S1 (ESI†) also contains the TGA data for the same films after they were immersed in water for 30 days under gentle agitation. We can confirm that no leaching of the NP occurred, supporting their chemical bonding to the cellulose fibrils. From the TGA analysis it can also be noted that only Fe$_2$O$_3$ acts as a catalyst in the pyrolysis reaction of the cellulose decreasing its degradation temperature by about 50 °C.

Fig. S2 (ESI†) depicts TEM images of the nanoparticles collected from the supernatant of the reaction. Selected area electron diffraction (SAED) data is provided, confirming the crystal structure of metallic gold and silver, the anatase phase for the titania and maghemite for the iron oxide. Particle size histograms computed from TEM images resulted in mean particle sizes of 7.5, 7.1 and 7.1 nm for Au, TiO$_2$ and Fe$_2$O$_3$ respectively with a maximum polydispersity index of 23%. A bimodal distribution was observed in the case of Ag nanoparticles with mean sizes of 8.2 and 40 nm, whilst sporadic dendritic larger sizes were also observed.
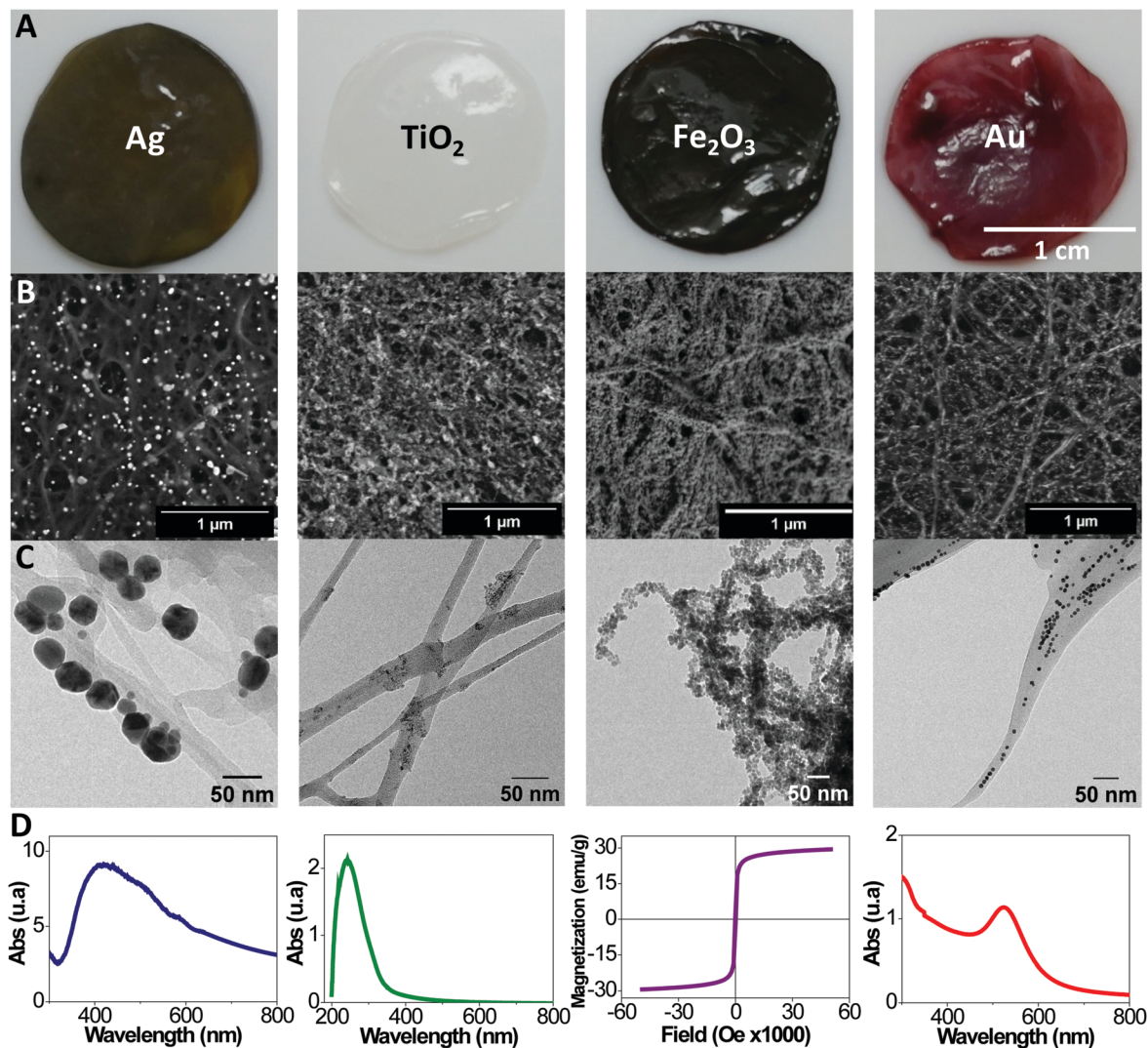
Fig. 1 (A) Bacterial cellulose films with different nanoparticles. (B) SEM images of the fibrils decorated with the nanoparticles. (C) TEM images of the fibrils where the size and distribution of the nanoparticles is more clearly apparent. (D) UV-VIS absorption spectra of each nanocomposite. In the case of the BC/Fe₂O₃, the magnetization curve is shown instead.

Fig. 1D illustrates a functional characteristic of each film. Plasmon absorption bands are observed for BC/gold and BC/silver films respectively. The BC/Au shows a maximum at 525 nm as expected for $\sim$10 nm gold particles.[34] A broad band for the BC/Ag, with a maximum at 420 nm and a smaller shoulder at 520 nm, indicates a larger particle size distribution for this material, and the presence of some anisotropic shaped particles such as triangles, hexagons and rods. Interestingly, by combining several plasmonic nanoparticles in one film or layering films of different metals, a multiplasmon film could be assembled. UV-absorption with a maximum at 242 nm is characteristic for the BC/TiO₂ composite. In turn, the BC/Fe₂O₃ film displays superparamagnetic behaviour due to the superparamagnetic character of the small iron oxide nanoparticles decorating the cellulose fibrils. A saturation magnetization of 30 emu g^{-1} is measured for the nanocomposite film, which is a rather high value for a nanocomposite with a non-magnetic matrix.

Next, we investigate the interfacial adhesion of two wet and native BC films dried on top of each other at 60 °C between two polytetrafluoroethylene (PTFE) plates using a Dynamic Mechanical Analysis (DMA) instrument. Fig. 2A shows a photograph of the resulting bilayer. Note that in order to perform the measurements half of the film is dried using a non-sticky paper between the two layers to prevent self-adhesion in this region. A SEM image of the bilayer cross section shows a smooth and continuous surface (Fig. 2B). The interface boundary between the two layers is not visible even in an enlargement of the cross section (inset of Fig. 2B). Thus, after drying, the two films look as a single thicker one.

Fig. 2C shows the peeling force as a function of the displacement. The curve depicts the behaviour of an increased load to achieve the initial displacement and more constant load with increasing displacement as the layers are peeled apart. We hypothesize that the drying facilitates a better adhesion towards the edges of the films so that the peeling crack is
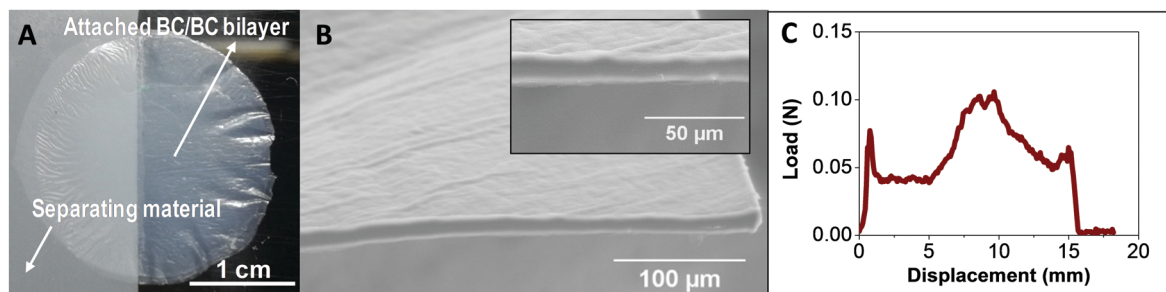
Fig. 2 (A) Set-up for a peeling test sample. The BC films were dried at 60 °C one above the other and between PTFE plates. Half of the sample was well attached and half was dried with a non-sticking paper in between to be able to attach the two ends of the layers to the test machine. (B) SEM image of the cross section of the bilayer. Inset is a magnification of the cross section. The interface of the two films is not visible. (C) Force vs. displacement curve, the area under the curve represents the interfacial energy needed to separate the BC films after drying.

arrested and propagation continues inside one of the layers rather than at the interface between them. That is the reason we are able to observe increased forces at the second middle of the sample i.e., at displacements of 10 and 15 mm (Fig. S3 (ESI†) contains a video of the peeling test experiment represented in Fig. 2C). A mean value for interfacial energy of 46 J m^{-2} was computed by integrating the area under the curve averaged from three independent experiments. This value is about twice the value previously reported for microfibrillated cellulose films from plants.[35]

To gain insight into the microscopic nature of cellulose–cellulose adhesion, we performed a series of molecular dynamics simulations (see ESI† for technical details). In our simulations, we consider in full atomistic detail the adhesion of two elementary crystalline cellulose fibrils of 6 nm length (18 144 atoms), as shown in Fig. 3A. We then studied two situations, namely, the case of two fibrils in water (full hydration with ∼16 000 water molecules) and

the case of dry conditions (no water). First, we determined their preferred configuration at 25 °C after adhesion (i.e. with the two fibrils in contact). The obtained equilibrium configuration shows substantial differences between the wet and dry scenarios (Fig. 3B and C). In the fully hydrated case, the two fibrils are in close proximity along a narrow strip but separated by water molecules, whereas in dry conditions the two fibrils adhere having a large contact surface along the fibrils. In dry conditions, the two fibrils tend to form aligned fibril–fibril hydrogen bonds, extending along the crystal structure. On the contrary, in the fully hydrated case, the two fibrils interact forming hydrogen bonds with water molecules at the cost of reducing the number of fibril–fibril hydrogen bonds.

Once the equilibrium configurations were determined, we performed pulling simulations in which the two fibrils were separated, allowing the calculation of the adhesion force as the
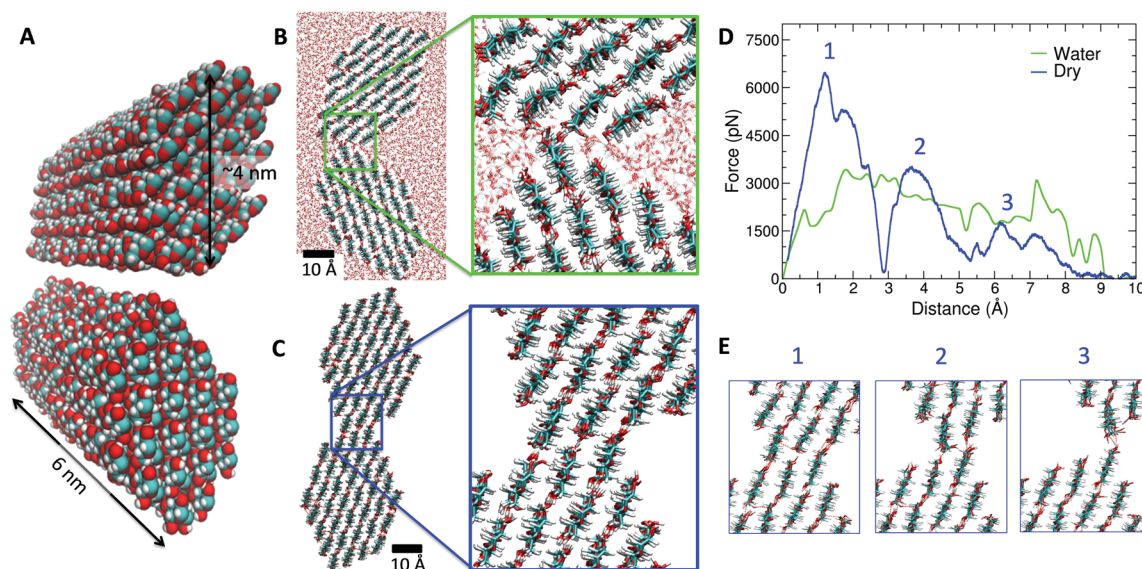

Fig. 3 MD simulation results at 25 °C. (A) Image of the atomic model for two bacterial cellulose fibrils with atoms shown in van der Waals size. The colour scheme is CPK (O in red, C in cyan and H in white). (B) Cross section view of the equilibrated configuration of the two fibrils in water at 25 °C. (C) Same as (B) but in dry conditions (no water). The inset denoted the increased contact surface, as compared with (B). (D) Adhesion force between the fibrils (in picoNewton, pN) as a function of the separation between the fibrils obtained in biased MD simulations in dry (blue line) and wet (green line) conditions. In dry conditions, three different particular events are indicated with numbers in the force curve. (E) Snapshots of the fibril–fibril interface corresponding to the events indicated by numbers in the force curve in (D). All snapshots were made using the VMD program.[36]

force required to detach completely the fibrils. In Fig. 3D, we show the force needed to detach the fibrils in both cases (full hydration and dry fibrils), from contact as starting position (configurations shown in Fig. 3B and C) to full separation. In dry conditions, simulations indicate that a force of ∼6500 pN is required to separate the fibrils (first peak highlighted in Fig. 3D). Interestingly, the dry fibrils separate in three stages (see the three peaks indicated in Fig. 3D), corresponding to the three alignments of hydrogen bonds between the fibrils shown in Fig. 3E. Each stage or event indicated in Fig. 3E corresponds to a peak in the force curve (Fig. 3D). In the first stage, a force of ∼6500 pN is required, whereas a smaller force of ∼2000 pN is needed in the third (and last) stage with only one hydrogen bond per contact to break (see Fig. 3E). In the simulations with fully hydrated cellulose fibrils, one third of the force (∼2000 pN) is required to separate the two fibrils and the three stages or events observed in the pulling of dried fibrils (Fig. 3E) do not appear. As discussed above, the number of hydrogen bonds between hydrated fibrils is smaller than in the case of dry conditions due to the competition between fibril–fibril and water–fibril hydrogen bonds. Thus, our atomistic simulations of crystalline cellulose fibrils provide a physical, microscopic mechanism for the increase of adhesion energy due to drying. According to our simulations, it is due to a stronger contact and a larger number of hydrogen bonds between fibrils favoured by the absence of water. The value of the maximum force observed in Fig. 2C (∼0.10 N) is comparable with having ∼10^7 aligned fibril–fibril contacts in dry conditions as the ones observed in Fig. 3C. Other complex factors not considered in the model (contacts in different orientations, entanglements, pore swelling/contraction) might also modulate the value of adhesion forces, but their consideration in the simulations is beyond the capabilities of atomistic models.

To elucidate if BC films containing nanoparticles also display such strong self-adhesive behaviour, two BC films with inorganic nanoparticles were dried together (Fig. 4A). Peel off tests were undertaken for bilayers either combining the same metal (BC/Au–BC/Au, BC/Ag–BC/Ag), two different metals (BC/Au–BC/Ag) or a semiconductor and a metal (BC/TiO$_2$–BC/Ag). From one side, the inclusion of nanoparticles in the BC fibrils increases the roughness of the film as estimated from AFM data in the case of BC/TiO$_2$ (rms roughness values: ∼0.20 μm for BC/TiO$_2$ and ∼0.08 μm for BC). On the other hand, nanoparticles might obstruct hydrogen–hydrogen interaction by either spacing the fibrils or decreasing the amount of hydroxyls on the cellulosic fibril surface. The BC/Ag–BC/TiO$_2$ bilayer resulted in an adhesion energy equal to the neat BC bilayer (46 J m^{-2}). This indicates that the hindering effects from the NPs decoration are compensated by the increase in roughness. Slightly smaller values are found by the BC/Au–BC/Au (33 N m^{-1}) and the BC/Au–BC/Ag bilayers (34 J m^{-2}) suggesting that the polymeric surfactants used in the metal nanoparticles synthesis (polyvinylpyrrolidone for silver, oleylamine for gold) may influence the strength of adhesion between two layers. A significantly smaller value (10 J m^{-2}) was found for the silver bilayer. We believe that the larger size of the silver nanoparticles inhibits a more intimate contact of the bacterial cellulose nanofibrils upon drying. Interestingly, confocal microscopy of the bilayer BC/Ag with BC/TiO$_2$ shows an integrated interface between the two films where the interface cannot be distinguished even though the image is obtained with the film submerged in water (rewetted). Fig. 4 collects the information regarding the bilayered materials. The flexibility during manual bending of all BC/nanoparticle dried films and of the bilayers was comparable to that of pristine BC, except for BC/Fe$_2$O$_3$, which showed a more brittle behaviour. This is attributed to the higher particle content (4.7 vol%, which is more than twice the content in other BC/NP samples).

Finally, we extended the bilayer approach to a millefeuille construct comprising four BC layers, each containing a different type of inorganic nanoparticle. The resulting multifunctional material behave as one film (∼50 μm) with the different nanoparticles geometrically confined in each layer. Fig. 5 shows a BC/Ag–BC/TiO$_2$–BC/Fe$_2$O$_3$–BC/Au film, and Fig. S4 (ESI†) depicts other layering types confirming that the layers can be

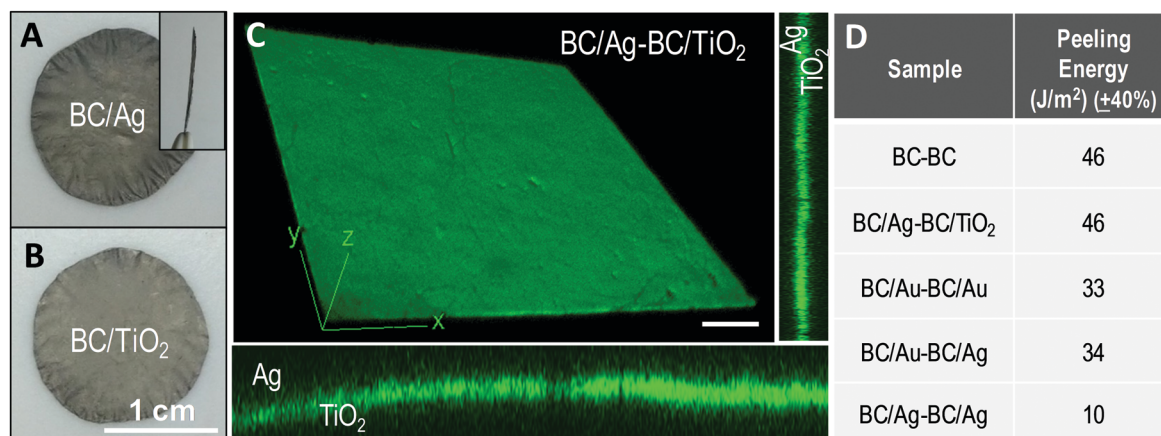| Sample	Peeling Energy (J/m²) (±40%)
BC-BC	46
BC/Ag-BC/TiO₂	46
BC/Au-BC/Au	33
BC/Au-BC/Ag	34
BC/Ag-BC/Ag	10

Fig. 4 (A) BC/Ag side of a bilayer BC/Ag–BC/TiO$_2$. Inset: Cross view of the thickness of the material (34 ± 3 μm). (B) BC/TiO$_2$ side of the same bilayer. (C) Confocal microscope image of the bilayer with the Ag layer on top. Thickness is 84 μm for the rewetted bilayer. The small images show the z-axis along x and y. Scale bar: 200 μm. (D) Peeling energy values for various bilayer combinations.
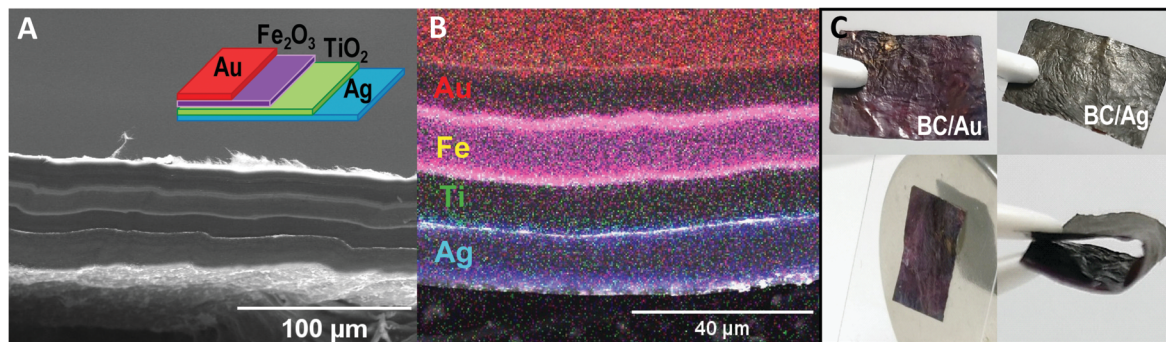
Fig. 5 (A) Millefeuille scheme of one of the possible configurations and SEM image of the cross section with the four layers of similar thicknesses visible due to the different contrasts of the nanoparticles. (B) EDX scan confirming the confined location of the different nanoparticles. (C) Upper panels: Millefeuille construct (1 cm × 1.5 cm) showing the two exterior, Au and Ag, layers. Lower panel: The millefeuille responding to a FeNdB permanent magnet (3 cm of diameter × 8 mm width) and the folded film without any apparent signs of mechanical failure.

laminated *ad libitum*. The layer stacking order would be determined by the final application envisioned for the material, *i.e.*, if antibacterial properties are important, then the BC/Ag layer will be placed outside, but if the relevant property is the plasmonic characteristic of the nanosilver then the BC/Ag layer can be a hidden one. Moreover, for some applications, the dielectric materials may be placed in between the metal layers (configuration shown in Fig. 5A) as it would be in a condenser set-up while for other applications, alternating the metals with the semiconductors might be the preferred sequence. Note that although the present concept is generic, the potential for laminated structures in multifunctional sensors may be particularly interesting. A SEM image of the millefeuille cross section with an electron dispersive X-ray (EDX) mapping analysis is depicted in Fig. 5B. The distribution of nanomaterials is

apparent. Fig. 5C shows the two sides of the millefeuille, BC/Au with the characteristic red/violet coloration of small gold particles and the reverse side with the grey colour given by the silver particles. Fig. 5C also shows the response of the material to a permanent magnet even when the BC/Fe_2O_3 is not in the outside part, as in this particular stacking order. The bending performance of the film is also illustrated.

Fig. S5 (ESI†) contains three videos showing the flexibility of the laminate construct and the good adhesion between the layers demonstrated by the absence of delamination during stringent manipulation (continuous pulling and bending) in the dry form and even after rewetting the construct for up to one week. Interestingly after one week in water and the harsh handling, a corner of the two metal layers was delaminated and by pulling it carefully, the films could be recovered intact (results not shown).
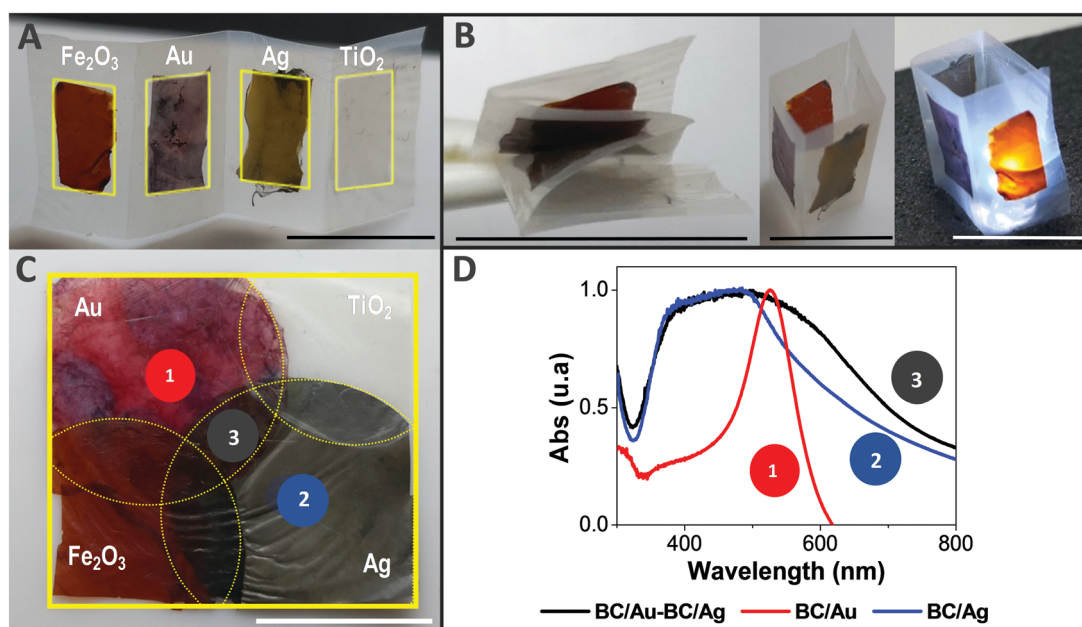

Fig. 6 (A) Planar configuration where BC films nanocomposited with metal and metal oxide nanoparticles are attached to a pristine BC film. (B) Versatility of the configuration made upon flexibility or creating 3D structures. (C) Configuration where single, double and triple multifunctionalities can be achieved on demand. (D) UV-VIS of the configuration shown in the scheme on (C). Scale bar = 1 cm.

Other interesting configurations are displayed in Fig. 6 to demonstrate the versatility of the approach. In the upper panel, Fig. 6A and B, a bilayer construct is displayed. It was made by drying layers of BC/NP over a pristine BC film, forming a strip of linearly arranged functionalities supporting the folding, or standing up as a 3D structure. The lower panel (Fig. 6C) shows another arrangement where single, double or triple functionalities coexist. Fig. 6D depicts the plasmon absorption spectra at the three points marked in Fig. 6C. Interestingly, in a single film one can measure different plasmon resonances spatially distributed or superimposed.

3. Conclusions

A concept of laminated multifunctional nanocellulose films has been developed, which is based on layers of bacterial cellulose strongly attached and with the fibrils in each layer decorated by specific inorganic nanoparticles. This millefeuille concept greatly enlarges the design space for multifunctional nanocellulose materials so that several nanotechnologies could be integrated in one material. The inorganic nanoparticles are strongly bonded to the fibrils by energy-efficient microwave-assisted synthesis routes. This method was previously reported for iron oxide, but was here extended to titania, gold and silver nanoparticles.

The proposed modular laminate could be *ad libitum* assembled by means of molecular scale cellulose–cellulose bond formation during cellulose film drying. This is possible because the unique properties of bacterial cellulose, namely, the nanometric dimensions of the fibrils allowing strong fibril–fibril interaction after drying. In addition, the 3D network nature of high-strength BC ribbons obtained from biosynthesis provides excellent mechanical integrity of the layers and of the final multifunctional laminate. The adhesion energy involved in the self-adhesive behaviour of two layers has been experimentally determined using peel off tests and related to values resulting from molecular dynamics simulations of different cases.

In this study, we have shown the viability of the methodology by presenting data for various ∼50 μm thick films constituted by up to four types of particles spatially confined in orderly manner across the film cross section. Thus, flexible nanocomposites from renewable sources with controlled nanoparticle properties were obtained. The topographic distribution of nanoparticles was controlled, as well as the volume fraction of particles within the porous scaffold, using simple approaches. The presented route paves the way to combining multiple functionalities and geometrical shapes in flexible cellulose-based substrates. Only a few examples of the concept have been outlined here, but multifunctional sensors, nanostructured devices and reactors for multiple catalytic effects are of interest, where specific functions are confined to spatially well-defined locations.

Conflicts of interest

There are no conflicts to declare.

Acknowledgements

References

1 A. Espinha, C. Dore, C. Matricardi, M. I. Alonso, A. R. Goñi and A. Mihi, *Nat. Photonics*, 2018, **12**, 343–348.

2 F. Li, E. Mascheroni and L. Piergiovanni, *Packag. Technol. Sci.*, 2015, **28**, 475–508.

3 Y. H. Jung, T.-H. Chang, H. Zhang, C. Yao, Q. Zheng, V. W. Yang, H. Mi, M. Kim, S. J. Cho, D.-W. Park, H. Jiang, J. Lee, Y. Qiu, W. Zhou, Z. Cai, S. Gong and Z. Ma, *Nat. Commun.*, 2015, **6**, 7170.

4 T. Tronser, A. Laromaine, A. Roig and P. A. Levkin, *ACS Appl. Mater. Interfaces*, 2018, **10**, 16260–16269.

5 D. Klemm, B. Heublein, H.-P. Fink and A. Bohn, *Angew. Chem., Int. Ed.*, 2005, **44**, 3358–3393.

6 D. Klemm, E. D. Cranston, D. Fischer, M. Gama, S. A. Kedzior, D. Kralisch, F. Kramer, T. Kondo, T. Lindström, S. Nietzsche, K. Petzold-Welcke and F. Rauchfuß, *Mater. Today*, 2018, **21**, 720–748.

7 T. Abitbol, A. Rivkin, Y. Cao, Y. Nevo, E. Abraham, T. Ben-Shalom, S. Lapidot and O. Shoseyov, *Curr. Opin. Biotechnol.*, 2016, **39**, 76–88.

8 D. Abol-Fotouh, B. Dörling, O. Zapata-Arteaga, X. Rodríguez-Martínez, A. Gómez, J. S. Reparaz, A. Laromaine, A. Roig and M. Campoy-Quiles, *Energy Environ. Sci.*, 2019, DOI: 10.1039/c8ee03112f.

9 Y. Guo, K. Zheng and P. Wan, *Small*, 2018, **14**, 1704497.

10 A. Laromaine, T. Tronser, I. Pini, S. Parets, P. A. Levkin and A. Roig, *Soft Matter*, 2018, **14**, 3955–3962.

11 L. G. Greca, J. Lehtonen, B. L. Tardy, J. Guo and O. J. Rojas, *Mater. Horiz.*, 2018, **5**, 408–415.

12 M. Zeng, A. Laromaine and A. Roig, *Cellulose*, 2014, **21**, 4455–4469.

13 M. Kaushik and A. Moores, *Green Chem.*, 2016, **18**, 622–637.

14 H. Golmohammadi, E. Morales-Narváez, T. Naghdi and A. Merkoçi, *Chem. Mater.*, 2017, **29**, 5426–5446.

15 H. M. C. Azeredo, M. F. Rosa and L. H. C. Mattoso, *Ind. Crops Prod.*, 2017, **97**, 664–671.

16 N. Lin and A. Dufresne, *Eur. Polym. J.*, 2014, **59**, 302–325.

17 H. Wei, K. Rodriguez, S. Renneckar and P. J. Vikesland, *Environ. Sci.: Nano*, 2014, **1**, 302–316.

18 W. Hu, S. Chen, J. Yang, Z. Li and H. Wang, *Carbohydr. Polym.*, 2014, **101**, 1043–1060.

19 S. Pal, R. Nisi, M. Stoppa and A. Licciulli, *ACS Omega*, 2017, **2**, 3632–3639.

20 A. Alonso-Díaz, J. Floriach-Clark, J. Fuentes, M. Capellades, N. S. Coll and A. Laromaine, *ACS Biomater. Sci. Eng.*, 2019, DOI: 10.1021/acsbiomaterials.8b01171.

21 N. Dal'acqua, A. B. De Mattos, I. Kringes, M. B. Pereira, H. Da Silva Barud, S. J. L. Ribeiro, G. C. S. Duarte, C. Radtke, L. C. Almeida, M. Giovanela, J. Da Silva Crespo and G. Machado, *J. Phys. Chem. C*, 2015, **119**, 340–349.

22 M. Chen, H. Kang, Y. Gong, J. Guo, H. Zhang and R. Liu, *ACS Appl. Mater. Interfaces*, 2015, **7**, 21717–21726.

23 S. Khan, M. Ul-Islam, W. A. Khattak, M. W. Ullah and J. K. Park, *Cellulose*, 2015, **22**, 565–579.

24 C. J. Smith, D. V. Wagle, H. M. O'Neill, B. R. Evans, S. N. Baker and G. A. Baker, *ACS Appl. Mater. Interfaces*, 2017, **9**, 38042–38051.

25 M. Zeng, A. Laromaine, W. Feng, P. A. Levkin and A. Roig, *J. Mater. Chem. C*, 2014, **2**, 6312–6318.

26 R. T. Olsson, M. A. S. A. Samir, G. Salazar-Alvarez, L. Belova, V. Ström, L. A. Berglund, O. Ikkala, J. Nogués and U. W. Gedde, *Nat. Nanotechnol.*, 2010, **5**, 584–588.

27 M. Vural, B. Crowgey, L. C. Kempel and P. Kofinas, *J. Mater. Chem. C*, 2014, **2**, 756–763.

28 E. Hendrick, M. Frey, E. Herz and U. Wiesner, *J. Eng. Fibers Fabr.*, 2010, **5**, 21–30.

29 S. Galland, R. L. Andersson, M. Salajková, V. Ström, R. T. Olsson and L. A. Berglund, *J. Mater. Chem. C*, 2013, **1**, 7963.

30 H. Zhu, S. Jia, T. Wan, Y. Jia, H. Yang, J. Li, L. Yan and C. Zhong, *Carbohydr. Polym.*, 2011, **86**, 1558–1564.

31 M. Baghbanzadeh, L. Carbone, P. D. Cozzoli and C. O. Kappe, *Angew. Chem., Int. Ed.*, 2011, **50**, 11312–11359.

32 I. Bilecka, P. Elser and M. Niederberger, *ACS Nano*, 2009, **3**, 467–477.

33 O. Pascu, E. Carenza, M. Gich, S. Estradé, F. Peiró, G. Herranz and A. Roig, *J. Phys. Chem. C*, 2012, **116**, 15108–15116.

34 W. Haiss, N. T. K. Thanh, J. Aveyard and D. G. Fernig, *Anal. Chem.*, 2007, **79**, 4215–4221.

35 H. Lönnberg, L. Fogelström, Q. Zhou, A. Hult, L. Berglund and E. Malmström, *Compos. Sci. Technol.*, 2011, **71**, 9–12.

36 W. Humphrey, A. Dalke and K. Schulten, *J. Mol. Graphics*, 1996, **14**, 33–38.